Heat flow and inferred ground surface temperature history at Tynong North, southeastern Australia

G. Beardsmore , M. Sandiford, K. Gordon, M. McLean, S. Egan & S. McLaren

Published online: 24 Aug 2017.

Submit your article to this journal ⬀

Article views: 12

View related articles ⬀

View Crossmark data ⬀

Taylor & Francis
Taylor & Francis Group

Heat flow and inferred ground surface temperature history at Tynong North, southeastern Australia

G. Beardsmore [ID], M. Sandiford, K. Gordon, M. McLean, S. Egan and S. McLaren

School of Earth Sciences, University of Melbourne, VIC 3010, Australia

ABSTRACT

Borehole temperature data have the potential to record historical variations in ground and air surface temperature, yet very few reliable, purpose-drilled, boreholes are available to explore such impacts, particularly in the southern hemisphere. The 400-m deep Tynong-1 borehole, approximately 65 km ESE of Melbourne, Australia, was drilled specifically to determine conductive heat flow and provides a unique dataset for evaluating ground surface temperature history in southeastern Australia. Steady-state conductive heat flow of 87 ± 1 mW m^{-2} was determined in the deeper borehole sections, with measured temperature profiles clearly demonstrating a progressive divergence of the observed temperature profile from the equilibrium model in the upper $\sim$150 m of the hole. We applied a Bayesian method employing a reverse jump Markov chain Monte Carlo search algorithm to explore the origins of this variation. Our results indicate a 2°C increase in ground surface temperature since 1800, after at least 500 years of relatively stable ground surface temperature. The inversion results are consistent with the trend of surface air temperature recorded in southeast Victoria by historical meteorological data since 1950. The inferred increase in ground surface temperature evident prior to 1950 is likely a cumulative effect of land clearing and a rise in surface air temperature.

Introduction

The potential for borehole temperature data to record variations in past ground surface temperature has long been recognised, and has been the subject of considerable research efforts around the world, particularly over the past two or three decades (e.g. Harris & Chapman, 1997; Majorowicz, Skinner, & Safanda, 2005; Pollack & Huang, 2000; Pollack, Huang, & Po-Yu, 1998; Roy & Chapman, 2012). The rate of diffusion of ground surface temperature (GST) variations into the ground depends on the subsurface properties of thermal conductivity and thermal diffusivity. Where these properties are known, the effect of specific changes in GST on the subsurface temperature field can be predicted with high precision. The inverse problem—inferring the surface temperature changes that caused an observed deviation in subsurface temperature—is inherently non-unique.

As recognised throughout the published literature, inference of GST histories from borehole temperature data is an ill-posed inverse problem that can be approached via a range of different numerical methods. These methods are broadly divisible into (1) regularisation-based and (2) Bayesian-inversion techniques. The results of any inversion depend to some extent on the method chosen, the details of the implementation, as well as the geological constraints built into the inversion. A number of authors have attempted to compare

different approaches (e.g. Eppelbaum, Kutasov, & Barak, 2006; Shen, Wang, Beltrami, & Mareschal, 1992) and to explore the impact of variations in geological and geophysical parameters such as borehole depth (e.g. Beltrami, Smerdon, Matharoo, & Nickerson, 2011) and uncertainties in measured thermal data (e.g. Hartmann & Rath, 2005).

The Bayesian approach avoids the tendency that Hartmann and Rath (2005) identified for regularisation approaches to almost always reconstruct a single, smooth GST history. Bayesian inference operates within a probabilistic framework to explore the full range of possible GSTs (constrained by the *a priori* assumptions) and determine the likelihood of each unique history based on how well that history explains the observed borehole temperature profile. Based on their likelihoods, some GST histories sampled from the *a priori* parameter space will be accepted and others rejected. The set of all acceptable GST histories forms an *a posteriori* probability density function describing the credible range of GST values through time. The width and shape of the distribution at any given time step give the 'most probable' GST at that time (that is, the GST that occurs in the greatest number of acceptable histories) but also, importantly, the credible range of GST at that time.

Huang, Pollack, and Shen (2000) previously employed borehole temperature logs and a probabilistic Bayesian

inference technique to infer likely GST histories at 616 sites globally, 57 of which were in Australia (Figure 1). For each of these sites Huang et al. (2000) derived linear GST histories for five century-long intervals from AD 1500 to 2000. When averaged around the globe, their results suggested a cumulative increase in mean global GST of about 1°C since AD 1500, but only a mean increase of 0.5°C for the 57 Australian sites. Their compiled data and individual interpretations of GST history are available online at https://www.ncdc.noaa.gov/paleo/borehole.

Working with a large dataset, Huang et al. (2000) necessarily made certain simplifying assumptions. For example, they assumed constant thermal conductivity with depth for each location. This assumption introduced random errors into their individual inversions, as few (if any) of the boreholes intersected rocks of homogenous thermal conductivity. To filter the effect of local random errors on individual inversions, Pollack, Huang, and Smerdon (2006) averaged the inferred GST histories of all 57 Australian boreholes investigated by Huang et al. (2000). The mean inferred GST history for Australia from Pollack et al. (2006) correlates well with the recorded increase in mean surface air temperature in Australia over the period 1900–1972 (1972 being the average date of the temperature logs upon which the surface temperature inversions were based).

The precision and accuracy of a GST inversion improves (that is, the mean inversion result lies closer to the 'true' GST history and the range of likely histories narrows) with increased quality of subsurface heat flow data. Essential thermal property data include measurements of temperature gradient, thermal conductivity and heat generation from within a thermally stabilised borehole but opportunities to collect well-characterised borehole thermal data to constrain a GST inversion are rare. The borehole Tynong 1, drilled in west Gippsland in 2011, provided one such opportunity because the borehole was designed and drilled specifically for surface heat flow determination, and the local geology is lithologically uniform, allowing thermal conductivity and heat production rates to be well characterised.

Tynong 1

Granite Power Limited drilled Tynong 1 (38°03′50″S, 145°38′05″E) over five weeks from 23 January to 4 March 2011 at Tynong North, approximately 65 km ESE of the city of Melbourne, Victoria (Figure 1). The borehole was sited specifically to intersect a large, homogenous granite pluton of Late Devonian age (Geological Survey of Victoria, 1997), locally referred to as the Tynong Granite (Figure 2).
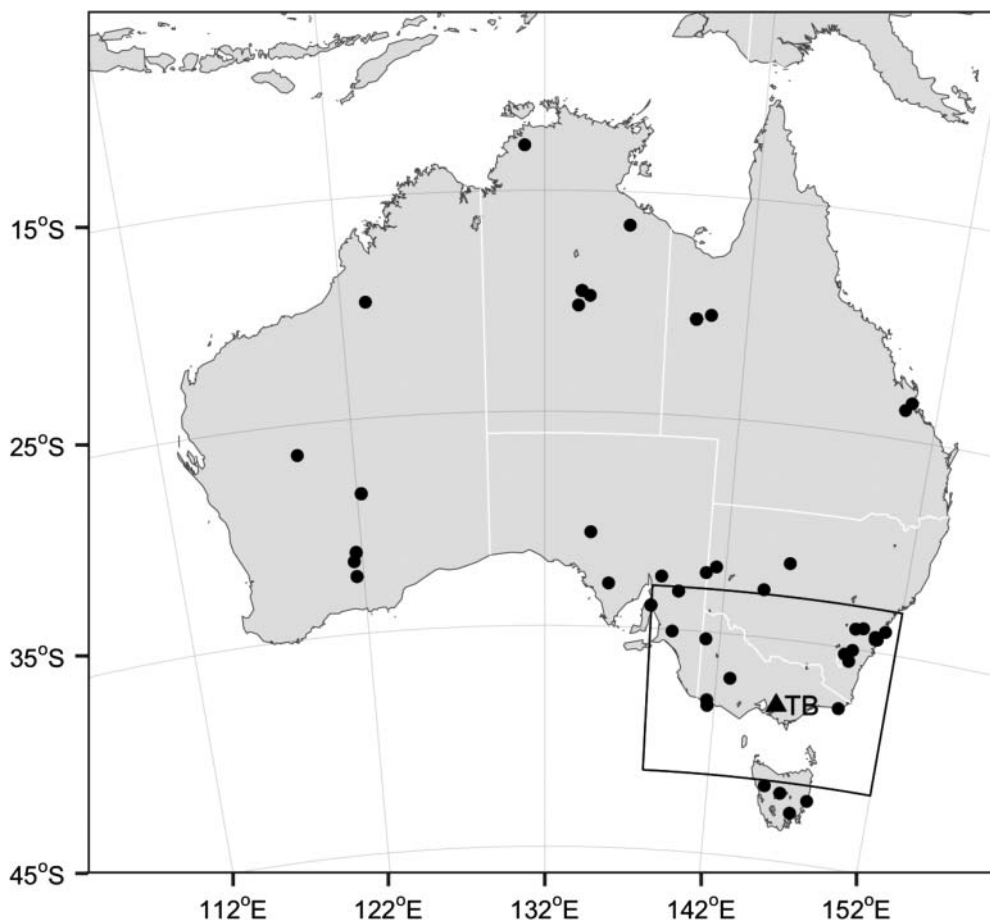

Figure 1. Locations of borehole temperature inversion sites from Huang et al. (2000). Eight locations represent multiple, closely spaced sites. Inset shows area covered by Figure 7. TB, Tynong 1 borehole.
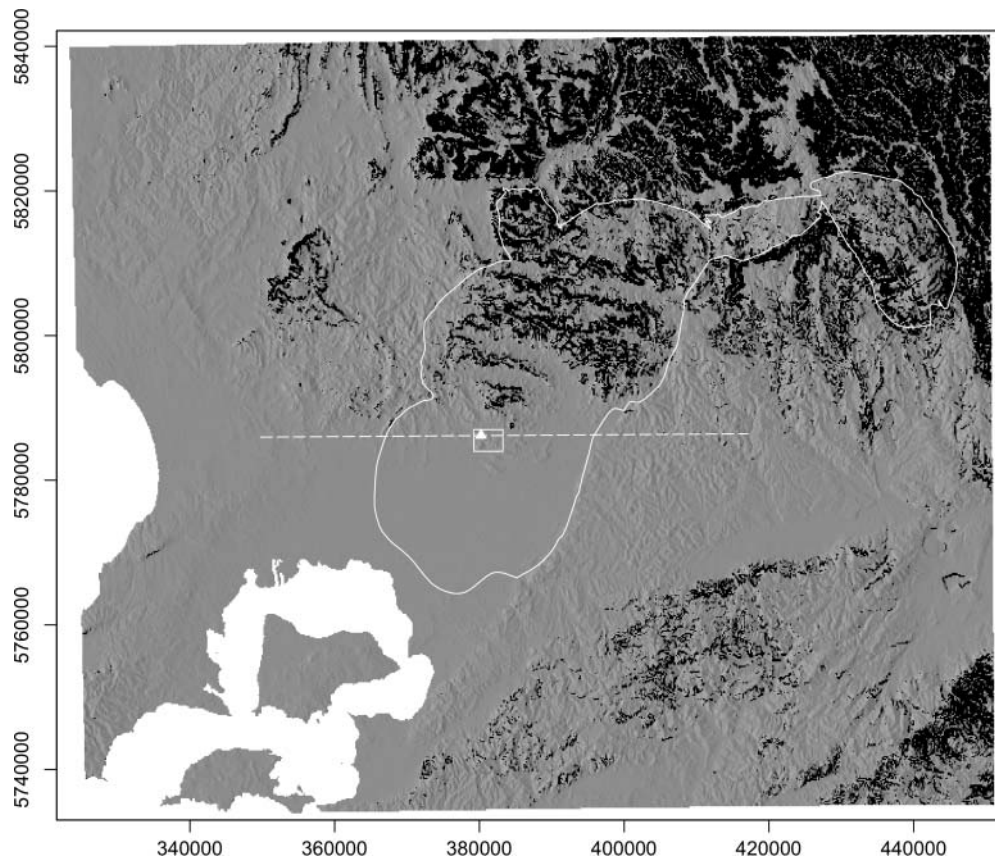
Figure 2. Location of Tynong 1 (white triangle) within the Tynong Granite (white outline) on the southern slopes of the Great Dividing Range (background topographic image). Dashed line shows location of gravity model in Figure 3. White rectangle shows extent of Figure 6. Shading is illuminated from the west, with slopes greater than 15° shown in black.

The Tynong Granite intrudes a thick sequence of marine clastic sediments comprising the Upper Ordovician Mt Easton Shale underlying Silurian to Lower Devonian turbidites of the Jordan River Group (McLean, Morand, & Cayley, 2010). Vandenberg et al. (2006) inferred a maximum thickness of 12–14 km for this folded 'Melbourne Zone' sequence from cross-sections drawn through areas of extensive outcrop, although its thickness near Tynong 1 is less well constrained. Cayley, Taylor, Vandenberg, and Moore (2002) argued that the Melbourne Zone rests upon a suite of Proterozoic to Cambrian mafic–ultramafic rocks called the Selwyn Block, which underlies a large area of central Victoria, Bass Strait and Tasmania. The Selwyn Block outcrops within a 100 km radius of Tynong 1 at Phillip Island (~60 km SW of Tynong 1), Waratah Bay (~95 km SSE of Tynong 1) and along the Governor Fault (~95 km NE of Tynong 1), so the Tynong Granite may intersect it at relatively shallow depth beneath Tynong 1.

The Tynong Granite has an average measured density of 2.63 g cm^{-3} (Skladzien, 2007) and is associated with a significant low gravity anomaly. McLean et al. (2010) interpreted the gravity data along an east–west profile passing about 10 km to the north of Tynong 1 as reflecting a granite plug ~4 km thick in the west, increasing to ~10 km thick in the east. We

generated a new east–west gravity section passing directly through Tynong 1 using the same parameters as McLean et al. (2010). A credible but conservative model (Figure 3) to explain the observed gravity requires at least 7 km of Tynong Granite intruded into 2–5 km of Jordan River Group turbidite (2.674 g cm^{-3}) and Mt Easton Shale (2.707 g cm^{-3}) above Selwyn Block basement (3.0 g cm^{-3}). While non-unique, we argue that this model defines a minimum thickness of Tynong Granite. The Jordon River Group has been mapped in detail (e.g. Haydon, Skladzien, & Cayley, 2006; Haydon, Skladzien, & Morand, 2006) and its thickness provides a robust modelling constraint. If the granite were interpreted to be < 7 km thick, the gravity data could only be matched with a thinner sequence of Jordon River Group than mapped. Thus, available gravity data verify that the Tynong Granite is a massive, regionally extensive body.

Thermal conductivity contrast between the Tynong Granite and the rocks into which it intruded is likely to be low. The average thermal conductivity of the granite is about 3.3 Wm^{-1} K^{-1} (see below). Antriasian, Taylor, Maher, Harrison, and Sandiford (2015) listed thermal conductivity measurements for many Victorian Paleozoic rocks, some of which serve as analogues for the Tynong Granite host rocks. Ordovician shales of the Castlemaine Group (analogue for the Mt Easton Shale) average 2.8 Wm^{-1} K^{-1}.
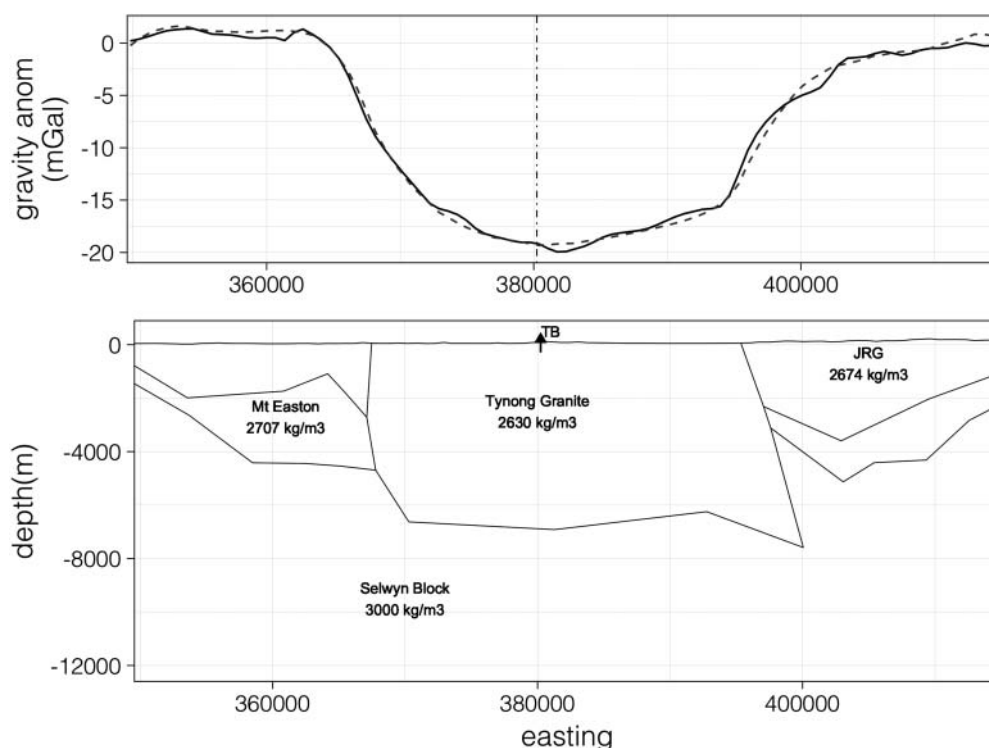
Figure 3. Credible but conservative gravity forward model passing east–west through Tynong 1. Top: Observed (solid) and modelled (dashed) Bouguer gravity anomaly. Below: 10 km-thick 2D section that produces the modelled gravity response. JRG, Jordon River Group. Eastings in MGA Zone 55.

Paleozoic turbidites around the state (analogue for Jordon River Group) average 3.5 Wm^{-1} K^{-1}. Selwyn Block proxy rocks average 3.5 Wm^{-1} K^{-1}. We infer from these values, and the distance that Tynong 1 was drilled from the edges of the granite, that heat-refraction effects will be negligible over the borehole depth.

Tynong 1 was drilled with a primary purpose to estimate the rate of heat flow supplied from the mantle and lower crust. Drilling records indicate that Tynong 1 passed through 14 m of clay and clay-rich soil and 11 m of weathered granite before penetrating unweathered granite from a depth of 25 m to its total depth of 400 m (Granite Power Ltd, 2011). The homogeneity of the penetrated granite, a lack of groundwater intersecting the borehole, and the distance of the borehole from the edges of the granite, combine to make the borehole an ideal source for heat flow data. The borehole was completed with steel casing so that it would remain accessible during the period of thermal re-equilibration following drilling. A near complete core was also recovered from 25 m depth to the final depth.

Thermal property data

The optimal data sets for a heat flow measurement are a high-precision equilibrium temperature (or temperature gradient) log and thermal conductivity measurements on core from the corresponding section. A full interpretation of heat flow is aided by measurements of radiogenic heat generation within the section. Each of these data sets was collected from Tynong 1.

Temperature logs

Different operators, using different tools and logging protocols, collected a total of seven temperature logs from the borehole at various times following cessation of drilling (Table 1; Figure 4). Generally, temperatures within the borehole would be expected to converge on equilibrium with the surrounding rock at increasing times after drilling. The University of Melbourne (UoM) collected logs 1, 2, 3, 4 and 7. Logs 2 and 4, collected as the tool was pulled back up the borehole, recorded noticeably higher temperatures than logs 1 and 3 collected on descent. Log 7 was collected using the same tool as logs 1, 2, 3 and 4, while descending the borehole. The temperature profile had notably cooled and stabilised in the intervening 100 days since log 4 was collected. Different operators (Hot Dry Rocks Pty Ltd; HDR) collected logs 5 and 6 using a different tool. Log 6 is slightly cooler and more stable than

Table 1. Temperature logs collected from Tynong 1.

Log no.	Date	Days since end of drilling	Operator[a]	Top	Bottom	Spacing	Direction
1	24 Mar	20	UoM	0.96 m	396.17 m	1 cm	Down
2	24 Mar	20	UoM	1.59 m	397.28 m	1 cm	Up
3	4 Apr	31	UoM	0.96 m	397.10 m	1 cm	Down
4	4 Apr	31	UoM	0.08 m	397.26 m	1 cm	Up
5	21 Apr	48	HDR	0 m	398 m	1 m	Down
6	12 May	69	HDR	0 m	398 m	1 m	Down
7	13 Jul	131	UoM	1.96 m	396.27 m	1 cm	Down

[a]UoM, University of Melbourne, School of Earth Sciences; HDR, Hot Dry Rocks Pty Ltd.

log 5, probably owing to the additional 21 days of thermal equilibration since drilling.

The HDR and UoM logs collected the longest times after drilling (log 6 and log 7, respectively) differed by as much as 0.17°C in the upper part of the well, probably owing to differences in tool calibration. The calibration of the HDR tool was well documented and traceable to the Australian National Measurement Institute, so we adopted log 6 as the most reliable temperature log for subsequent modelling.

Thermal conductivity

Thermal conductivity was measured parallel to the vertical axes of 12 core specimens across the full vertical section of granite intersected in Tynong 1. For each specimen, three disks were cut to determine mean conductivity and standard deviation. Each disk was evacuated under >95% vacuum for a minimum of 3 h before being saturated at atmospheric pressure for a minimum of 16 h. Thermal conductivity was measured with a divided bar apparatus calibrated for samples of various size and thickness following a procedure subsequently published by Popov, Beardsmore, Clauser, and Roy (2016). All measurements were made at 25°C (±2°C). As our modelling assumed one-dimensional vertical heat flow, we calculated the effective vertical thermal conductivity for each specimen as the harmonic mean and one standard deviation of the measured conductivities (Table 2).

Heat generation

Three core specimens (GPL108, GPL113 and GPL118) were analysed for potassium, thorium and uranium concentrations using a whole-rock fusion method. The results were combined with density measurements on the same specimens following a method described by Beardsmore and Cull (2001) to estimate the natural rate of radiogenic heat generation in the granite (Table 3). The small number of measurements was a commercial decision by the borehole operator. The goal was to determine a mean value of heat generation for the granite, with an assumption of low variance. The two deepest specimens returned very similar values, while the shallowest appeared relatively leached of thorium and enriched in potassium, consistent with near-surface weathering effects. Here, the close agreement in the calculated radiogenic heat generation of the two deeper specimens appears to validate the assumption of low variance, and their mean value, 5.85 μW m^{-3}, is taken as the average for the full thickness of the Tynong Granite. The sensitivity of our steady-state heat flow estimate and GST history inversion to this value are discussed in the relevant sections below.

Thermal diffusivity

Thermal diffusivity controls the depth to which cyclic surface temperature perturbations distort the subsurface temperature gradient. Thermal diffusivity (κ) is related to thermal conductivity (λ), density (ρ) and specific heat
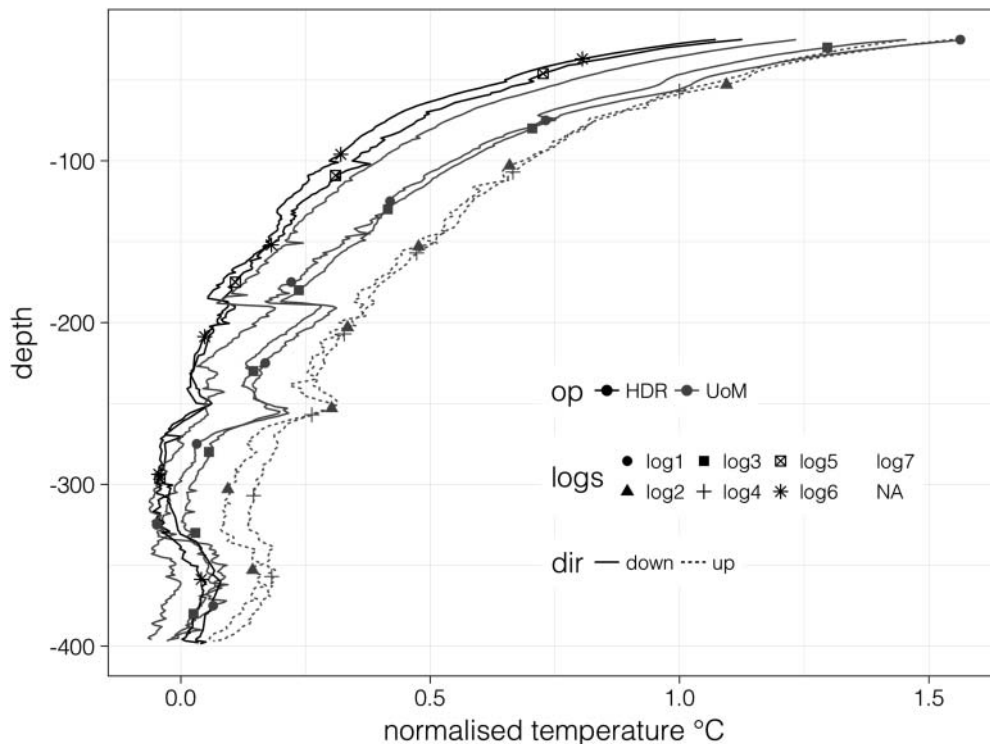

Figure 4. Temperatures recorded by the seven logs listed in Table 1, normalised to a linear regression fit to log 5 temperatures deeper than 200 m. The regression geotherm is 14.09 + 25.59 z°C, where z is the depth in kilometres.

Table 2. Thermal conductivity data for the Tynong Granite, Tynong 1.

Lithology	Depth from (m)	Depth to (m)	Sample ID		Conductivity (W m⁻¹ K⁻¹), harmonic mean, standard deviation	
GRANITE, white, coarse-grained	25.52	25.61	GPL107	A	3.14	
				B	2.96	3.06 ± 0.09
				C	3.08	
GRANITE, grey, medium-grained	52.10	52.30	GPL108	A	3.46	
				B	3.41	3.41 ± 0.06
				C	3.35	
GRANITE, grey, coarse-grained	74.84	74.97	GPL109	A	2.80	
				B	2.86	2.83 ± 0.03
				C	2.83	
GRANITE, white, coarse-grained	100.12	100.35	GPL110	A	3.28	
				B	3.02	3.13 ± 0.13
				C	3.10	
GRANITE, grey-brown, medium-grained	123.84	124.03	GPL111	A	3.46	
				B	3.38	3.42 ± 0.04
				C	3.44	
GRANITE, grey-brown, medium–coarse-grained	150.20	150.40	GPL112	A	3.58	
				B	3.54	3.55 ± 0.02
				C	3.55	
GRANITE, grey, medium–coarse-grained	175.71	176.06	GPL113	A	3.53	
				B	3.56	3.55 ± 0.01
				C	3.55	
GRANITE, grey, medium–coarse-grained	225.03	225.24	GPL114	A	3.52	
				B	3.53	3.52 ± 0.01
				C	3.50	
GRANITE, white, coarse-grained, trace Fe pyrite	276.22	276.60	GPL115	A	3.09*	
				B	3.30	3.32 ± 0.01
				C	3.35	
GRANITE, grey-pink, coarse-grained	325.32	325.56	GPL116	A	3.04	
				B	3.21	3.17 ± 0.12
				C	3.28	
GRANITE, grey-brown, coarse-grained	375.33	375.57	GPL117	A	3.40	
				B	3.44	3.44 ± 0.04
				C	3.47	
GRANITE, grey, medium–coarse-grained	386.52	385.76	GPL118	A	3.49	
				B	3.58	3.51 ± 0.05
				C	3.47	

Table 3. Uranium, thorium and potassium concentration derived from whole-rock fusion analyses.

Specimen number	Density (g cm⁻³)	Uranium concentration (ppm)	Thorium concentration (ppm)	Potassium concentration (%)	Heat generation (μW m⁻³)
GPL108	2.62	11.8	10.2	4.10	4.07 ± 0.05
GPL113	2.62	12.2	35.6	3.64	5.89 ± 0.07
GPL118	2.63	11.7	35.7	3.95	5.81 ± 0.07

Density was measured using Archimedes' principle.

capacity (c_p) by:

$$\kappa = \lambda / \left(\rho c_p \right) \qquad (1)$$

We estimated a mean value of thermal diffusivity of 1.56 ± 0.08 × 10⁻⁶ m² s⁻¹ for the shallow granite (<100 m) from measurements of thermal conductivity (3.22 W m⁻¹ K⁻¹; ± 1% uncertainty) and density (2.62 g cm⁻³; ± 1% uncertainty), and an estimate of specific heat capacity (790 J kg⁻¹ K⁻¹; ± 3% uncertainty).

No samples were collected or measured from the clay-rich soil or the weathered zone that sit above the solid granite. We estimated the thermal diffusivity of this interval at 1.1 ± 0.1 × 10⁻⁶ m² s⁻¹ using the range of estimates of conductivity, density and specific heat capacity of wet and dry soils listed in The Engineering Toolbox (retrieved 6 December 2016 from www.engineeringtoolbox.com).

We applied these estimates of thermal diffusivity to our investigation of the depth of influence of daily and seasonal temperature cycles described below. The inversion algorithm for investigating GST history inferred thermal diffusivity from the thermal conductivity profile in Table 2 (corrected for *in situ* temperature as described below), density of 2.62 g cm⁻³ and specific heat of 790 J kg⁻¹ K⁻¹ using Equation 1.

Modelled heat flow

Steady-state heat flow

The steady-state conductive temperature profile is the baseline from which transient departures are defined. The steady-state conductive temperature profile in Tynong 1 can be inferred by finding the values of surface heat flow, Q_0 Wm⁻², and mean surface temperature, T_0°C, that produce the best fit

between observed and predicted thermal gradient at each depth using the following equation (Beardsmore & Cull, 2001):

$$Q_0 = \lambda_d \times [\delta T/\delta z]_d + \int_0^d A(z)\mathrm{d}z \qquad (2)$$

where λ_d and $[\delta T/\delta z]_d$ are the thermal conductivity (W m^{-1} K^{-1}) and thermal gradient (°C m^{-1}), respectively, at depth, d (m), and $\int_0^d A(z)\mathrm{d}z$ is the cumulative heat generation (W m^{-2}) between the surface and depth, d.

Thermal conductivity is sensitive to temperature. The values in Table 2 were measured at 25°C (±2°C), but for greatest precision these were corrected for *in situ* (logged) temperature before applying Equation 2. We applied the temperature correction of Vosteen and Schellschmidt (2003):

$$\lambda_T = \lambda_0 / [0.99 + T(a - b/\lambda_0)] \qquad (3)$$

where λ_0 = thermal conductivity (W m^{-1} K^{-1}) at 0°C, λ_T = thermal conductivity at T°C, and 'a' and 'b' are empirically derived constants (respectively, 0.0030 and 0.0042 for crystalline rocks, and 0.0034 and 0.0039 for sedimentary rocks.)

Table 4 lists the modelled depth intervals and *in situ* rock property values for Tynong 1. Figure 5 shows the temperature profile generated using Equation 2, which best fits the temperatures observed in the deeper section of log 6. The model implies a steady-state heat flow, $Q_0 = 86.8$ mW m^{-2}, and equilibrium mean surface temperature, $T_0 = 14.0$°C. Variations of ±50% on the assumed internal heat generation affect the value of Q_0 by ±0.6 mW m^{-2} and have no impact on T_0 to one decimal place.

The equilibrium model matches the observed temperature at the eight interval boundaries from 148 m to the bottom of

Table 4. Modelled thermal conductivity and heat-generation profile in Tynong 1, from measured values and assumed interval boundaries.

Depth to top (m)	*In situ* conductivity (W m^{-1} K^{-1})	Heat generation (μW m^{-3})
0	2.55 ± 0.50	1.0
14	3.07 ± 0.50	2.3
25	3.11 ± 0.09	4.1
30	3.47 ± 0.06	4.1
67	2.87 ± 0.03	5.85
80	3.17 ± 0.13	5.85
110	3.47 ± 0.04	5.85
148	3.59 ± 0.02	5.85
163	3.59 ± 0.01	5.85
207	3.55 ± 0.01	5.85
242	3.34 ± 0.01	5.85
321	3.18 ± 0.12	5.85
362	3.45 ± 0.04	5.85
378	3.52 ± 0.05	5.85

Interval boundaries were picked to coincide with observed discontinuities in thermal gradient.

the borehole with a root-mean-square misfit of 0.026°C, confirming the borehole is in conductive thermal equilibrium at those depths but above 148 m the observed temperature is increasingly higher than that predicted by the equilibrium model. The equilibrium model suggests that a previous stable GST of 14.0°C had increased by more than 1°C at the time of temperature logging. There are three possible mechanisms for the inferred increase in ground temperature: solar heating cycles, land clearing and long-term atmospheric temperature rise.

Solar heating cycles

Regular cycles of ground surface heating and cooling from the daily and seasonal passage of the sun diffuse into the ground and perturb the thermal gradient at shallow levels, but are effectively negligible and can be ignored at depths
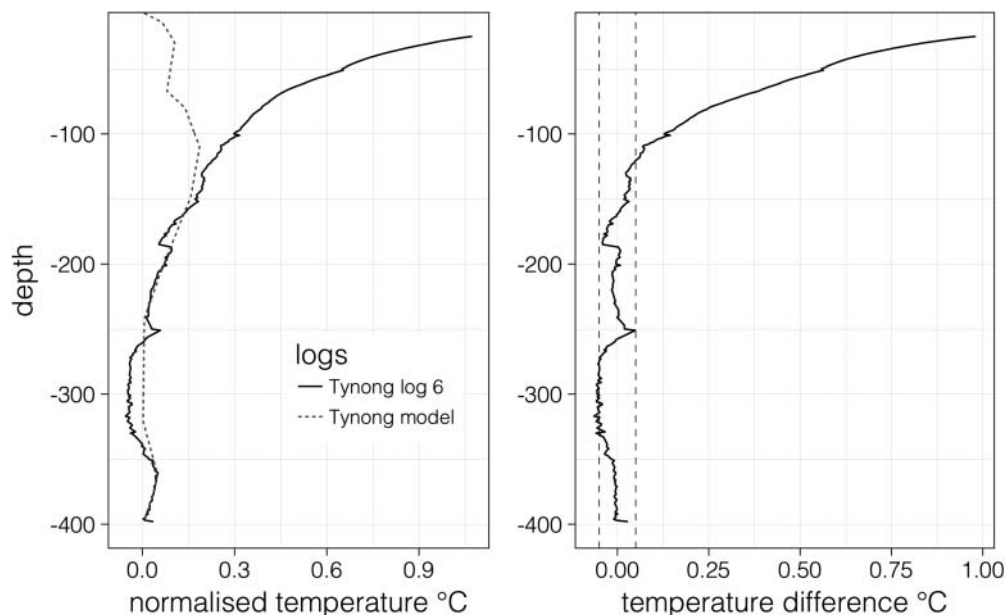

Figure 5. (a) Modelled equilibrium temperature in Tynong 1 for a surface heat flow $Q_0 = 86.8$ mW m^{-2} and surface temperature = 14.0°C (dashed line) and observed log 6 (solid line), both normalised against a reference geotherm (14.06 + 25.06 z°C). (b) Difference between the observed log (log 6) and the modelled equilibrium temperature field. Dashed lines show ±0.05°C bounds.

greater than one 'effective wavelength' of diffusion (Beardsmore & Cull, 2001). The effective wavelength (w_e) is a function only of thermal diffusivity (κ) and the period (P) of the heating cycle:

$$w_e = (4\pi P \kappa)^{1/2} \qquad (4)$$

Diffusivity of the soil at Tynong North was estimated above at $1.1 \pm 0.1 \times 10^{-6}$ m^2 s^{-1}. From Equation 4, the daily cycle of solar heating and radiative cooling of the ground surface, with a period of 24 h (86 400 s), has an effective wavelength of 1.09 ± 0.05 m. The seasonal cycle of summer heating and winter cooling, with a period of 365 days (3.16×10^7 s), has an effective wavelength of 20.9 ± 1.0 m. That is, the impact of the daily cycle on subsurface temperatures is negligible below about one metre, while the seasonal cycle is unlikely to affect temperatures at the top of the solid granite at 25 m. The divergence between the observed temperature profile and the equilibrium model between 25 m and 148 m in Tynong 1 cannot therefore be attributed to solar cycling.

Permanent changes in GST

The dominant mechanisms controlling thermal energy exchange between the atmosphere and the ground surface are:

1. Direct solar radiation onto the ground:

$$R_S.(1 - a_T).\cos(\mathbf{I}) \qquad (5)$$

where R_S = incident solar radiation (W m^{-2}), $\mathbf{I}$ = the angle (°) incident rays make normal to the ground, and a_T = the total albedo of the ground (dimensionless).

2. 'Grey box' radiation from the ground:

$$\varepsilon.\sigma.\mathbf{T_0}^4 \qquad (6)$$

where ε = 'emissivity' of the surface (dimensionless), σ = the Stefan-Boltzmann constant = 5.670400×10^{-8} W m^{-2}K^{-4}, and $\mathbf{T_0}$ = absolute GST (K).

3. Diffuse atmospheric radiation onto the ground:

$$R_D.(1 - a_W) \qquad (7)$$

where R_D = diffuse radiation (W m^{-2}), largely in the infrared band at night but also ultraviolet during the day; a_W = the albedo of the ground at the relevant wavelengths (dimensionless).

4. Heat conduction across the air–ground boundary:

$$R.(\mathbf{T_a} - \mathbf{T_0}) \qquad (8)$$

where $\mathbf{T_a}$ = surface temperature of the air (K), $\mathbf{T_0}$ = GST (K), and R = heat transfer coefficient (W m^{-2}K^{-1}). This is negative

(i.e. net flow of heat is from the ground to the air) when $\mathbf{T_0} > \mathbf{T_a}$.

The total heat flux (Q_t) from the atmosphere to the ground at any given time (ignoring condensation and evaporation) is the sum of these four effects; direct solar radiation minus 'grey box' radiation from the Earth's surface plus diffuse atmospheric radiation plus or minus direct heat conduction across the air–ground boundary:

$$Q_t = R_S.(1 - a_T).\cos(\mathbf{I}) - \varepsilon.\sigma.\mathbf{T_0}^4 + R_D.(1 - a_W)$$
$$+ R.(\mathbf{T_a} - \mathbf{T_0}) \qquad (9)$$

A net positive Q_t results in an increase in GST (i.e. $\mathbf{T_0}$) at a rate proportional to the volumetric heat capacity of the ground. Conversely, a net negative Q_t results in a cooling GST. The heating or cooling stops when $\mathbf{T_0}$ reaches a value that makes Q_t once again equal zero. Under pseudo-steady-state conditions, cumulative fluxes of heat into and out of the ground are equal over the course of a year, and the annual mean GST remains constant. However, Equation 9 shows that a permanent change in any of several variables must result in a permanent change in mean annual GST to maintain thermal equilibrium. These variables include the cumulative incident solar radiation, surface albedo (total and/or wavelength-specific), emissivity, heat transfer coefficient, the cumulative diffuse atmospheric radiation and/or the mean annual surface air temperature.

Changes in land use

A permanent change in land use can affect several of the variables mentioned above. For example, land clearing generally increases the amount of incident radiation (R_S and R_D) that reaches the ground, as well as changes the albedo (a_T and a_W), emissivity (ε) and heat transfer coefficient (R) of the ground surface. Draining or flooding an area can likewise have a dramatic and permanent effect on albedo, emissivity and heat transfer coefficient. Changes in land use tend to be relatively instantaneous and permanent, resulting in a step change to a new equilibrium GST. For example, Beardsmore (2005) inferred that GST increased by 1°C two years prior to a temperature log at a site in Western Australia, which coincided with clearing of native vegetation for the drilling pad.

Tynong North is in the southern foothills of Victoria's Great Dividing Range (Figure 2). The area was most likely covered with riparian woodland or lowland forest prior to European settlement on the site in 1904 but has since been cleared for grazing. Records are vague about the precise time of clearing around the site of Tynong 1, but it can be constrained to the first half of the 20th century, with aerial photographs from 1947 (Figure 6) showing the area mostly cleared. There have been no subsequent significant changes in land use between clearing and the collection of thermal data from Tynong 1.

Clearing of the native woodland vegetation would have instantaneously (at our temporal scale of interest) and permanently altered the albedo and emissivity of the ground
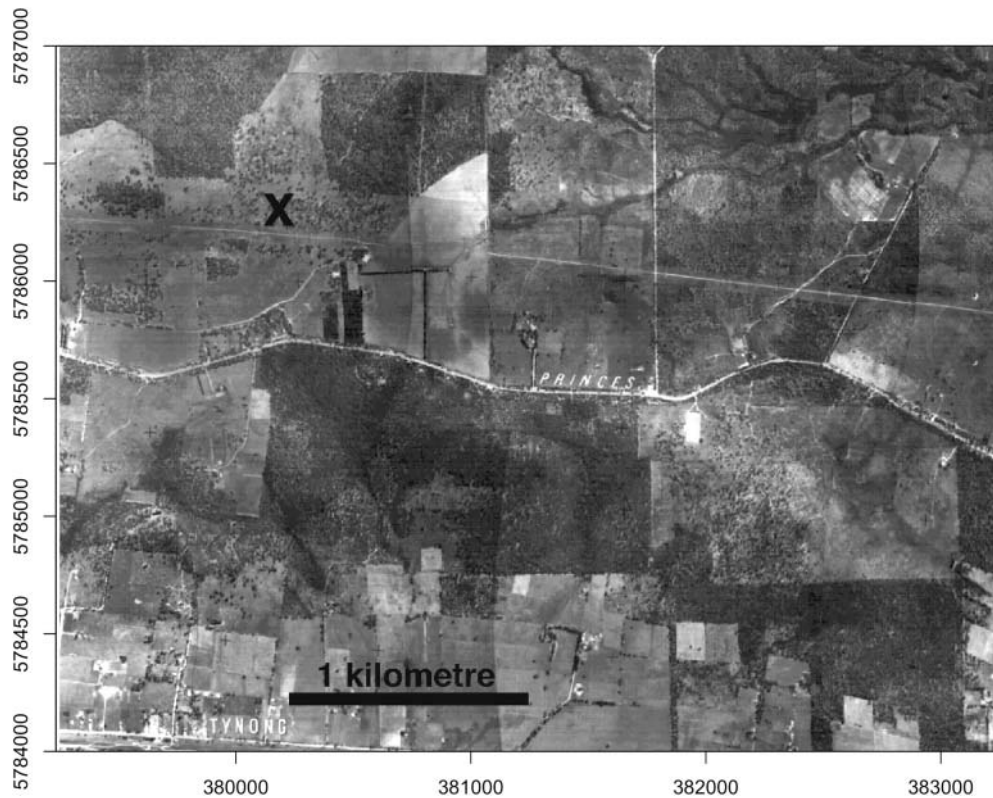
Figure 6. Extent of land clearing around Tynong North in 1946. The area around Tynong 1, shown by the X in the top left of the image, is already mostly cleared. Modified after Department of Lands and Survey (1948).

surface. A greater proportion of direct sunlight and atmospheric radiation would also have reached the ground after clearing and nocturnal radiative cooling rates probably decreased because grasslands typically have lower emissivity than forests (Snyder, Wan, Zhang, & Feng, 1998). The net effect would most likely have been a step increase in mean annual GST sometime between 1904 and 1947. For an assumed thermal diffusivity of 1.56×10^{-6} m^2 s^{-1}, a nominal $1°C$ rise in temperature within that period would be observable above $\pm$ $0.05°C$ noise to a depth of 150–200 m. This effect would be superimposed upon any longer-term, gradual change in GST owing to atmospheric warming.

Atmospheric warming

The gradual increase in the atmospheric concentration of CO_2 increases R_D, the amount of 'grey-box' infrared radiation reflected to the ground surface. This results in a gradual increase in mean annual GST from pre-warming equilibrium conditions and (over the long term) an equivalent increase in the mean surface air temperature, T_a. Changes in T_a can be inferred from meteorological records.

The Australian Bureau of Meteorology collects and maintains records of surface air temperature at many sites around Australia. Only a relatively small number of sites, however, provide data of sufficient longevity and quality to monitor long-term climatic effects. The peer-reviewed 'Australian Climate Observations Reference Network—Surface Air

Temperature' (ACORN-SAT) dataset uses best practice analytical techniques as well as digitised observational data to provide a daily record of Australian temperatures over the last century (Australian Government Bureau of Meteorology, 2016.) Records in the ACORN-SAT dataset provide a continuous, self-consistent, long-term record of daily maximum and minimum temperatures at 112 observation locations around Australia. Eleven of these sites are in Victoria, with Sale, Wilsons Promontory, Melbourne Regional Office and Laverton Royal Australian Air Force Base being the four sites closest to Tynong 1 (Figure 7). Relative to the 1960–1990 average, these four sites all record an increase of about $1°C$ in surface air temperature since 1950 (Figure 8).

Bayesian inference of GST history

We chose to follow the method of Hopcroft, Gallagher, and Pain (2007), who used a Bayesian-based reverse jump Markov chain Monte Carlo (RJ-MCMC) approach as described by Green (1995). Hopcroft et al. (2007) described the formulation of an *a priori* 'probability density function' (PDF) constraining the possible range of a set of variables defining the GST history. The GST history was defined as a series of discrete periods of linear GST change over a defined time interval, with degrees of freedom allowed over the number of discrete periods, the beginning and end times of each period (to one-year resolution), the magnitude of change in GST over each period, the uncertainty in the borehole temperature data and the
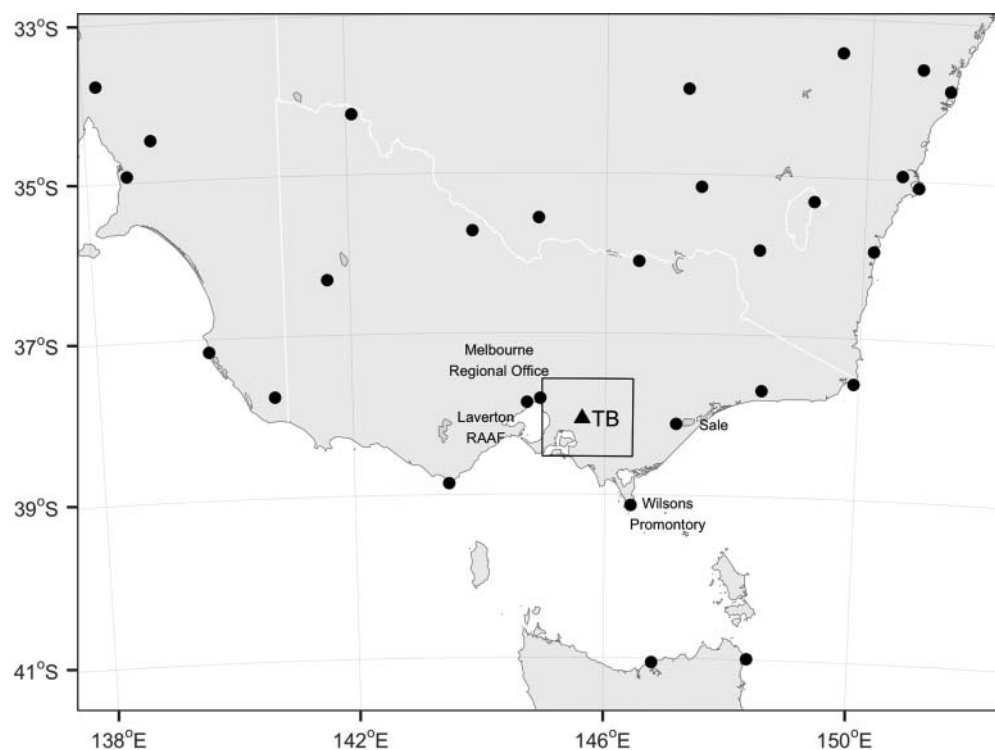
Figure 7. ACORN-SAT sites in southeastern Australia; labelled sites used for this analysis; TB, Tynong 1 borehole.

'background' heat flow and GST prior to the time when the borehole data provide resolution on GST changes.

The Bayesian approach is to calculate the temperature–depth profiles expected for many possible GST histories within the bounds of the *a priori* constraints, and to quantify the relative likelihood of each proposed GST history based on how well its predicted temperature–depth profile matches the observed temperature–depth profile.

Our diffusion model was constrained by available measured thermal property data, as described above, and compared against log 6 assuming an uncertainty of $\pm 0.05°C$ (one standard deviation) on the recorded temperatures. Within the
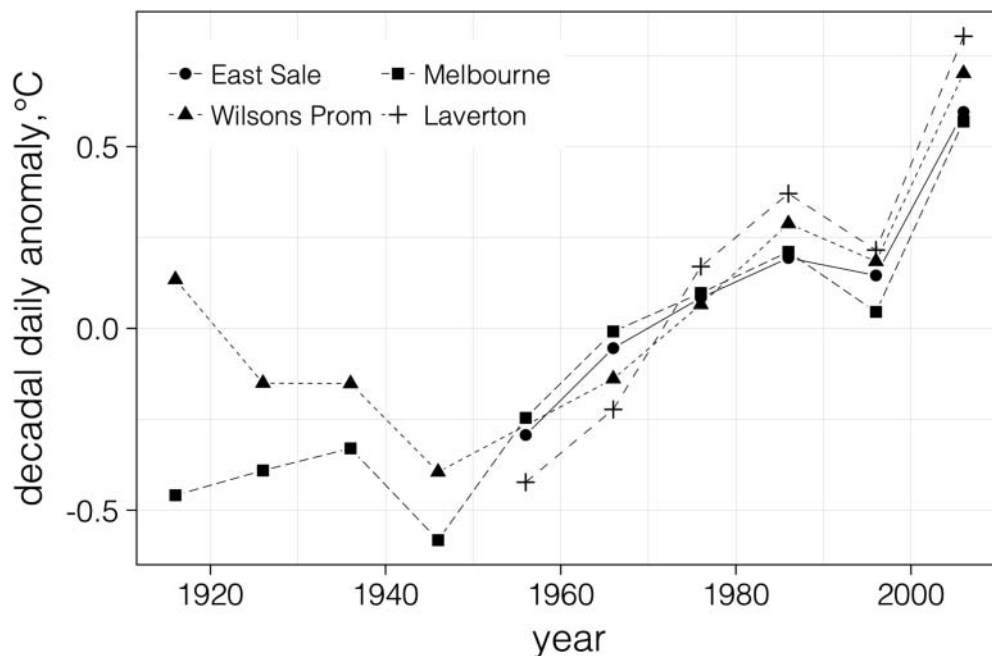

Figure 8. Decadal mean surface air temperatures, relative to 1960–1990 averages, as recorded at the four ACORN-SAT sites closest to Tynong 1.
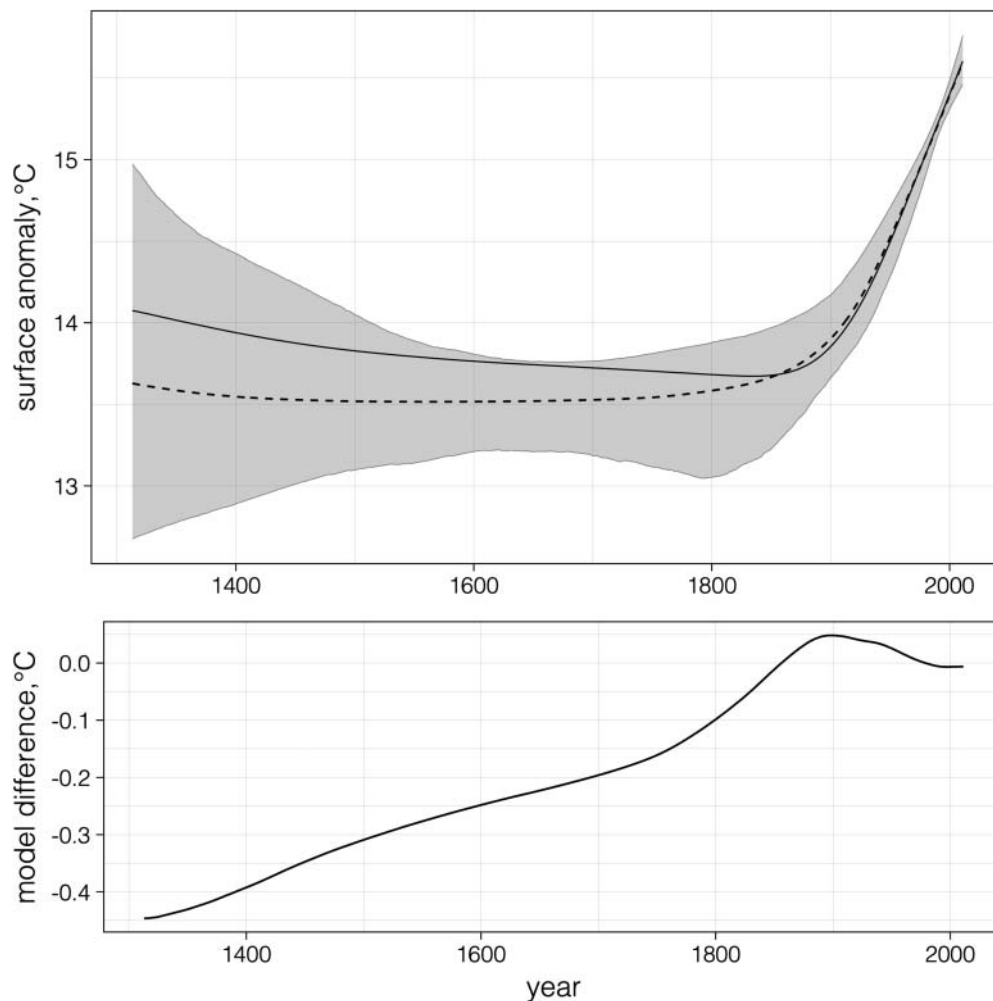
Figure 9. (Top) Bayesian inversion of 700-year GST history at Tynong 1. Solid line shows posterior mean GST history inferred from the log 6 temperature profile as recorded. Dashed line shows the posterior mean inferred GST history after correcting log 6 for internal heat generation. Shading shows the credible range (95%) of likely GST using the corrected log. (Bottom) Difference between the posterior mean GST histories inferred from the corrected and uncorrected temperature logs.

constraints of the *a priori* PDF, we allowed the software to infer the most probable range of GST histories over the preceding 700 years (AD 1310–2010). We followed the precedent of Hopcroft et al. (2007) for our prior distribution types, how we generated proposals and our proposal acceptance criteria. We set our initial estimates of pre-observation mean basal heat flow at 0.084 Wm^{-2} and pre-observation mean GST at 14.1°C, consistent with the reference geotherms assumed on Figures 4 and 5. The RJ-MCMC search ran for 500 000 iterations, with the first 50 000 discarded during the 'burn-in' process.

A weakness of the RJ-MCMC code that we employed was that it did not incorporate internal heat generation in its forward model calculations of subsurface temperature. The internal heat generation of the Tynong Granite (Table 3) is relatively high, and is likely to have had a measurable effect on the temperature profile in Tynong 1. The heat generated within the 375 m section of granite intersected by Tynong 1 accounts for 2.2 mW m^{-2} at the surface, or about 2.5% of the 86.8 mW m^{-2} steady-state heat flow. This effectively increases

the thermal gradient at the top of the granite by about 2.5% relative to the gradient at the base of the borehole. While this has a negligible effect on the calculated steady-state heat flow in the deeper portion of the borehole (see above), the RJ-MCMC code could 'interpret' the curvature of the geotherm as resulting from a decrease in GST over time. Indeed, the result of the inversion (solid curve on Figure 9) suggests gradual cooling of about 0.4°C over the AD 1310–1850 period, with a subsequent rise of about 2°C.

To test the sensitivity of the inversion to internal heat generation, we repeated the inversion on a synthetic temperature profile representing a scenario with zero internal heat generation. We produced the synthetic temperature profile by modelling two steady-state geotherms for the observed thermal conductivity profile in Tynong 1, surface heat flow 86.8 mW m^{-2} and surface temperature 14.0°C. One model assumed zero internal heat generation, and the other assumed 5.85 μW m^{-3} internal heat generation. We added the difference between the two modelled geotherms to the log 6 observed temperature profile to represent an equivalent

log with zero internal heat generation. The posterior mean of the resulting inversion (dashed line on Figure 9) suggested a more stable GST over the AD 1300–1800 period, but retained the inferred 2°C of warming since AD 1800. The posterior means of each inversion was well within the 95% credible limits of the other, indicating that the inversion is relatively insensitive to internal heat generation. To test the sensitivity of the outcome to the defined time interval of the inversion, we reduced the interval to 500 years. The results were not markedly different to the 700-year inversion.

In summary, the thermal data collected from Tynong 1 indicate steady-state conductive heat flow of 86.8 mW m^{-2} at depths greater than 148 m. This steady-state interval suggests a stable GST of 14.0°C, which is at least 1.5°C cooler than the mean GST at the time of temperature logging. The discrepancy is insensitive to internal heat generation and the time interval of the inversion, and almost certainly owing to a net increase in GST since the last period of relative thermal equilibrium.

Discussion

The purpose-drilled nature of Tynong 1 for measuring conductive heat flow provides a high level of confidence in our results. All relevant heat flow data are exceptionally well constrained, revealing a background heat flow of 87 ± 1 mW m^{-2} in the bore deeper than 150 m. We infer 1.5–2.6°C rise in GST since 1800, with 1.3–1.9°C of that rise since 1900 and 0.7–1.4°C since 1950. GST was probably stable between 1600

and 1800. The inversion results are insensitive (within the credible bounds) to internal heat generation and the time interval of the inversion. The expanding width of the credible range of GST prior to 1600 reflects the limits of resolution of the inversion imposed by the ±0.05°C uncertainty in the borehole temperature data.

While the inversion results suggest GST warming most likely commenced early in the first half of the 19th century, within the 95% credible interval no warming is required until about 1910. The minimum required rise in temperature is 1.7°C over the last three centuries, with at least 1.3°C accruing since 1900, while the maximum inferred rise in GST is 2.6°C since around 1800, with up to 1.9°C since 1900.

The precision of the heat flow data was insufficient to discriminate between the contributions of atmospheric warming and changes in land use to the inferred changes in GST. In other words, the diffusion of any step change in GST resulting from land clearing 70–105 years before temperature logging is indistinguishable (given the precision of the heat flow data) from the diffusion of longer-term gradual atmospheric changes. Furthermore, the inversion algorithm did not explicitly search for step changes in GST owing to changes in land use. Instead, we investigated the relative contributions of atmospheric warming and land use change to the inferred GST history by looking at correlations between the inferred GST history and ACORN-SAT surface air temperature records. We noted that the inferred GST history since 1950 correlates closely with the trend of the ACORN-SAT surface air temperature records (Figure 10). This period entirely post-dates the
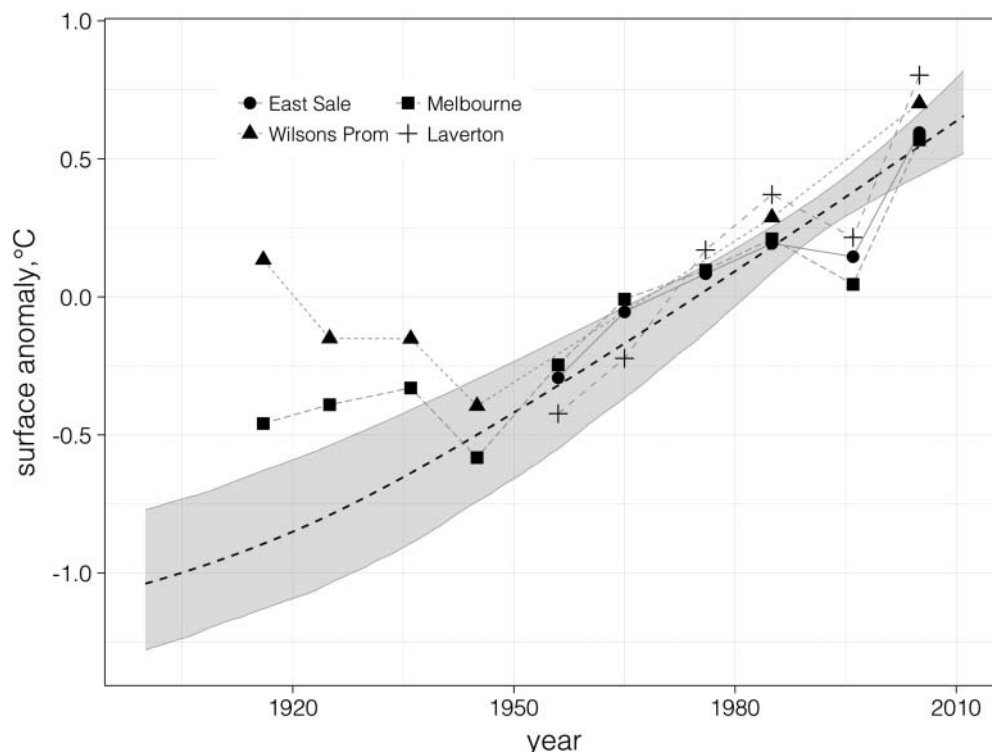

Figure 10. ACORN-SAT decadal averaged surface anomaly for the period 1910–2010 overlain on the posterior GST trend since 1910 inferred from Tynong 1 borehole temperatures (dashed line with grey shading of the credible range), relative to 1960–1990 averages.
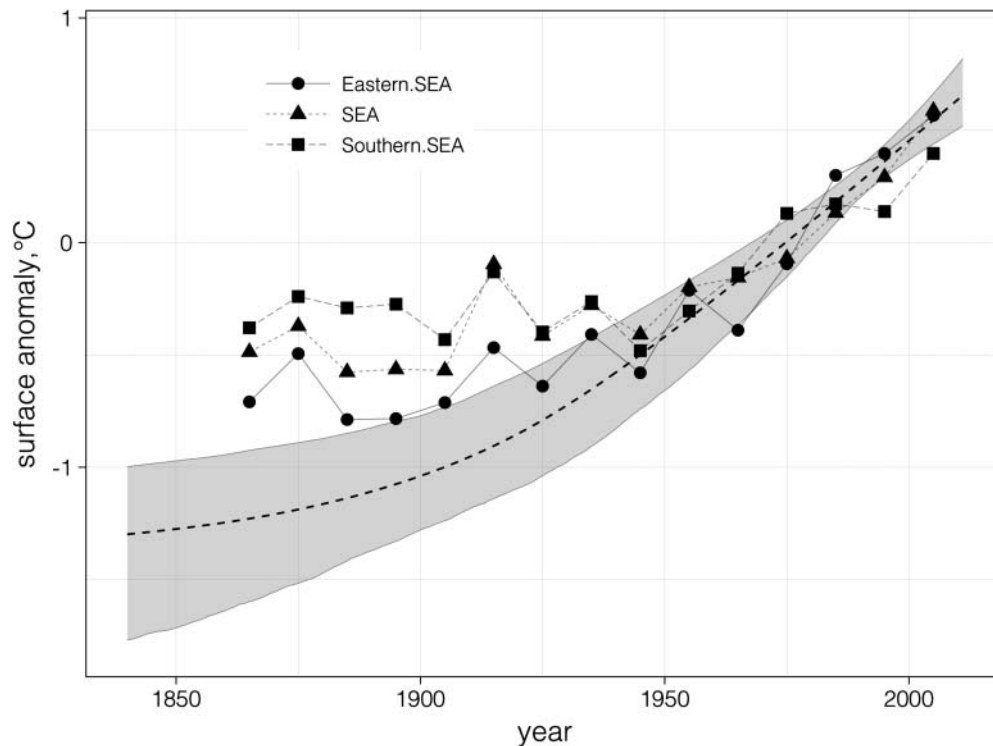
Figure 11. Reconstructed temperatures as decadal averaged surface anomaly from Ashcroft et al. (2012) for the AD 1860–2010 period overlain on the posterior GST trend since AD 1840 inferred from Tynong 1 borehole temperatures (dashed line with grey shading of the credible range). Surface anomaly measured relative to AD 1960–1990 averages.

last major change in land use, so the inferred increase in GST of 0.7–1.4°C since 1950 can be entirely attributed to increasing surface air temperature, consistent with the ACORN-SAT record over the same period.

Our inversion results suggest a divergence between GST warming and the ACORN-SAT surface air temperature record prior to 1940s. The divergence is corroborated by the reconstructions of surface air temperatures compiled by Ashcroft, Karoly, and Gergis (2012), who extended the quality assured SAT record for SE Australia back to 1860 and produced average records for southeastern Australia (SEA; 138–154°E, 24–40°S). For the decades from the 1860s to the 1940s, the Ashcroft reanalysis shows no significant surface air temperature warming, whereas our inversions imply a posterior mean warming of 0.75°C with a 95% credible range between 0.2 and 1.4°C (Figure 11).

Historical records place the major change in land use at Tynong in the period between 1904 and 1947, when the land was cleared for grazing. Given the close correlation between surface air temperature and inferred GST since 1950, we attribute the divergence between inferred GST and recorded SAT trends in the first half of the 20th century at least in part to the effect of this land clearing.

As such, we conclude that the net increase in GST inferred from the Tynong 1 temperature log is likely due to a combination of two causes; a step change in mean surface temperature

owing to land clearing between 1904 and 1947, and a gradual increase related to changing atmospheric conditions.

Huang et al. (2000) provided a good example of the ambiguities that remain when inverting poorly constrained heat flow data. They inferred ~2°C of GST cooling between 1800 and 1964 at Stawell, approximately 200 km WNW of Melbourne, and their nearest data point to Tynong 1. Their conclusion was based on a relatively high observed thermal gradient in the uppermost 100 m of the Stawell borehole and an assumption of uniform thermal conductivity (and diffusivity) with depth. Using their data and assumptions, we inferred ~1°C of GST cooling over the same period using the RJ-MCMC inversion algorithm (Figure 12). However, the assumptions of pure conduction and uniform thermal conductivity are not likely to be valid at this site, which is known to have a complicated surface geology, juxtaposing rocks with very different thermal properties (e.g. shales, granites, metamorphosed basalts). Alternative explanations for the high gradient include a lower thermal conductivity at shallow levels and advective heat transfer within the near surface. The data presented by Huang et al. (2000) are insufficient to discriminate between these possible explanations and a reduction in GST over time, and point to the necessity of purpose-drilled holes such as Tynong 1 (ideally in areas with no historical land use change) in obtaining robust records of GST changes.
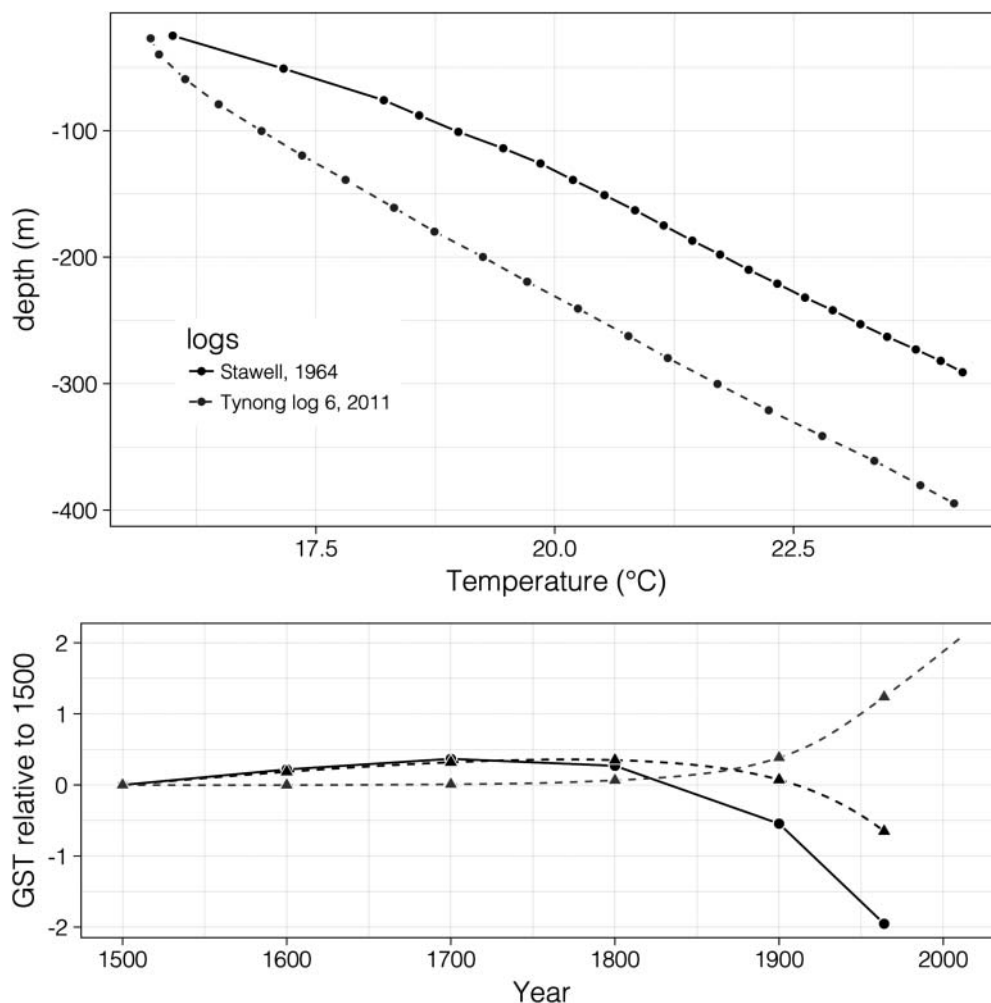
Figure 12. (a) Comparison of temperature logs from Stawell (data from Huang et al., 2000) and Tynong North (this study), Victoria. (b) Comparison of GST histories inferred for (1) black dots: Stawell (Huang et al., 2000), (2) black triangles: Stawell (this study) and (3) grey triangles: Tynong North (this study).

Disclosure statement

No potential conflict of interest was reported by the authors.

ORCID

G. Beardsmore http://orcid.org/0000-0003-4812-1146

References

Antriasian, A., Taylor, D., Maher, B., Harrison, B., & Sandiford, D. (2015). *Thermal conductivity measurements of Victorian rocks: Victorian Geothermal Atlas Report 2*. Geological Survey of Victoria Technical Record 2015/3. Melbourne, Vic: Geological Survey of Victoria.

Ashcroft, L., Karoly, D., & Gergis, J. (2012). Temperature variations of southeastern Australia, 1860–2011. *Australian Meteorological and Oceanographic Journal*, *62*, 227–245. Retrieved from http://www.bom.gov.au/amm/papers.php?year=2012

Australian Government Bureau of Meteorology. (2016). Long-term temperature record: Australian Climate Observations Reference Network – Surface Air Temperature (ACORN-SAT). Retrieved December 1, 2016, from http://www.bom.gov.au/climate/change/acorn-sat/documents/About_ACORN-SAT.pdf

Beardsmore, G. R. (2005). High-resolution heat-flow measurements in the Southern Carnarvon Basin, Western Australia. *Exploration Geophysics*, *36*, 206–215. doi:10.1071/EG05206

Beardsmore, G. R., & Cull, J. P. (2001). *Crustal heat flow: A guide to measurement and modelling*. Cambridge, UK: Cambridge University Press.

Beltrami, H., Smerdon, J. E., Matharoo, G. S., & Nickerson, N. (2011). Impact of maximum borehole depths on inverted temperature histories in borehole paleoclimatology. *Climate of the Past, 7*, 745–756. doi:10.5194/cp-7-745-2011

Cayley, R. A., Taylor, D. H., Vandenberg, A. H. M., & Moore, D. H. (2002). Proterozoic–Early Palaeozoic rocks and the Tyennan Orogeny in Central Victoria: The Selwyn Block and its tectonic implications. *Australian Journal of Earth Sciences, 49*, 225–254. doi:10.1046/j.1440-0952.2002.00921.x

Department of Lands and Survey. (1948). Photo-Map Drouin A4 or 860 A4 Zone 7. Aerial Survey of Victoria Series. Retrieved November 4, 2016, from http://services.land.vic.gov.au/maps/content/photomapwizard.

Eppelbaum, L. V., Kutasov, I. M., & Barak, G. (2006). Ground surface temperature histories inferred from 15 boreholes temperature profiles: Comparison of two approaches. *Earth Sciences Research Journal, 10*, 25–34. Retrieved from http://www.revistas.unal.edu.co/index.php/esrj/issue/view/2006

Geological Survey of Victoria. (1997). Warrigal, SJ 55-10, Edition 2. 1:250,000 Geological Map Series. Victorian Department of Natural Resources and Environment, May 1997. Retrieved from http://earthresources.efirst.com.au/Default.asp?c=93212

Granite Power Ltd. (2011). *Tynong Project—Final Technical Report for Rediscover Victoria Drilling Initiative Round 3* (unpublished). Victorian Department of Primary Industries, 24 May 2011. 52pp. Retrieved from http://earthresources.efirst.com.au/categories.asp?cID=3

Green, P. J. (1995). Reversible jump Markov chain Monte Carlo computation and Bayesian model determination. *Biometrika, 82*, 711–732. doi:10.2307/2337340

Harris, R. N., & Chapman, D. S. (1997). Borehole temperatures and a baseline for 20th-century global warming estimates. *Science, 275*, 1618–1621. doi:10.1126/science.275.5306.1618

Hartmann, A., & Rath, V. (2005). Uncertainties and shortcomings of ground surface temperature histories derived from inversion of temperature logs. *Journal of Geophysics and Engineering, 2*, 299–311. doi:10.1088/1742-2140/2/4/S02

Haydon, S. J., Skladzien, P. B., & Cayley, R. A. (2006). *Parts of Mansfield, Alexandra and Euroa 1:100 000 maps: Geological Interpretation of Geophysical Features Map*. Melbourne, Vic: GeoScience Victoria. Retrieved from http://earthresources.efirst.com.au/categories.asp?cID=11

Haydon, S. J., Skladzien, P. B., & Morand, V. J. (2006). *Parts of Matlock, Moe and Maffra 1:100 000 maps: Geological Interpretation of Geophysical Features Map*. Melbourne, Vic: GeoScience Victoria. Retrieved from http://earthresources.efirst.com.au/categories.asp?cID=11

Hopcroft, P. O., Gallagher, K., & Pain, C. C. (2007). Inference of past climate from borehole temperature data using Bayesian Reversible Jump Markov chain Monte Carlo. *Geophysical Journal International, 171*, 1430–1439. doi:10.1111/j.1365-246X.2007.03596.x

Huang, S., Pollack, H. N., & Shen, P. Y. (2000). Temperature trends over the past five centuries reconstructed from borehole temperatures. *Nature, 403*, 756–758. doi:10.1038/35001556

Majorowicz, J. A., Skinner, W. R., & Safanda, J. (2005). Ground surface warming history in northern canada inferred from inversions of temperature logs and comparison with other proxy climate reconstructions. *Pure & Applied Geophysics, 162*, 109–128. doi:10.1007/s00024-004-2582-6

McLean, M. A., Morand, V. J., & Cayley, R. A. (2010). Gravity and magnetic modelling of crustal structure in central Victoria: What lies under the Melbourne Zone? *Australian Journal of Earth Sciences, 57*, 153–173. doi:10.1080/08120090903416245

Pollack, H. N., & Huang, S. (2000). Climate reconstruction from subsurface temperatures. *Annual Review of Earth and Planetary Sciences, 28*, 339–365. doi:10.1146/annurev.earth.28.1.339

Pollack, H. N., Huang, S., & Po-Yu, S. (1998). Climate change record in subsurface temperatures: A global perspective. *Science, 282*(5387), 279–281. doi:10.1126/science.282.5387.279

Pollack, H. N., Huang, S., & Smerdon, J. E. (2006). Five centuries of climate change in Australia: The view from underground. *Journal of Quaternary Science, 21*, 701–706. doi:10.1002/jqs.1060

Popov, Y., Beardsmore, G., Clauser, C., & Roy, S. (2016). ISRM suggested methods for determining thermal properties of rocks from laboratory tests at atmospheric pressure. *Rock Mechanics and Rock Engineering, 49*, 4179–4207. doi:10.1007/s00603-016-1070-5

Roy, S., & Chapman, D. S. (2012). Borehole temperatures and climate change: Ground temperature change in south India over the past two centuries. *Journal of Geophysical Research, Atmospheres, 117*, D11105. doi:10.1029/2011JD017224

Shen, P. Y., Wang, K., Beltrami, H., & Mareschal, J. C. (1992). A comparative study of inverse methods for estimating climatic history from borehole temperature data. *Global and Planetary Change, 6*, 113–127. doi:10.1016/0921-8181(92)90030-E

Skladzien, P. (2007). *Compilation of rock densities for Victoria. Gold Undercover Report 5*. Melbourne, Vic: Geoscience Victoria.

Snyder, W. C., Wan, Z., Zhang, Y., & Feng, Y.-Z. (1998). Classification-based emissivity for land surface temperature measurement from space. *International Journal of Remote Sensing, 19*, 2753–2774. doi:10.1080/0143116982144977

Vandenberg, A. H. M., Cayley, R. A., Willman, C. E., Morand, V. J., Seymon, A. R., Osborne, C. R., … Sandford, A. C. (2006). *Walhalla–Woods Point–Tallangallook Special map area geological report*. Melbourne, Vic: Geological Survey of Victoria Report *127*. Retrieved from http://earthresources.efirst.com.au/product.asp?pID=168&cID=39

Vosteen, H.-D., & Schellschmidt, R. (2003). Influence of temperature on thermal conductivity, thermal capacity and thermal diffusivity for different types of rock. *Physics and Chemistry of the Earth, 28*, 499–509. doi:10.1016/S1474-7065(03)00069-X